Experimental and Numerical Research on a Design Concept of Two-stage Compression Inward-turning TBCC Inlet

Zhancang Hu[1], Yiqi Tang[2], Zhonglong Li[3], Zejun Cai[4], Zhenqi Sun[5], Chengxiang Zhu[6], Yancheng You[7]

Abstract

The inlet system plays a vital role in achieving the wide speed range flight based on the Turbine-Based Combined Cycle (TBCC) propulsion system. Developing reliable design methods and conducting detailed experimental studies for the TBCC inlet is imperative. In this paper, an inward-turning TBCC inlet working within $Ma_\infty=0\sim4$ was designed based on the two-stage compression basic flow field, and wind tunnel tests were conducted on a scaled model at the design point and several off-design points. The schlieren system and pressure acquisition system were employed to capture the flow structure and record the pressure data. At $Ma_\infty=4$, experimental pressure ratio distributions along the upper wall agree well with the numerical results, demonstrating the two-stage compression shock wave structure and validating the design concept. The maximum back pressure ratio and critical total pressure recovery coefficient were 76.56 and 0.506 at the design point, respectively, agreeing well with the simulation results of 76.03 and 0.505. Furthermore, during the tests, the inlet can start and work stably under subsonic $Ma_\infty=0.8$, supersonic $Ma_\infty=2$, and $Ma_\infty=3$, exhibiting good aerodynamic performance. These experimental results reveal the working characteristics of the inward-turning TBCC inlet within the wide speed range and effectively validate the design concept of the inlet employed in this work, promoting its engineering application.

Keywords: *Turbine-Based Combine Cycle (TBCC), Two-stage compression, Inward-turning inlet, Numerical simulation, Wind tunnel test*

Nomenclature

H_c – center body height
Ma_∞ – freestream Mach number
Ma_{exit} – outlet Mach number
p_∞ – freestream static pressure
δ_1 – first-stage compression angle
δ_2 – second-stage compression angle
ρ_∞ – freestream density
σ_{exit} – outlet total pressure recovery coefficient

π_k – outlet experimental pressure ratio
π_b – outlet numerical pressure ratio
Subscripts
exp – experimental result
num – numerical result
R – ramjet duct
T – turbine duct
∞ – freestream

1. Introduction

The air-breathing vehicle utilizing the Turbine-based Combined Cycle (TBCC) propulsion system [1-2] provides a possibility for horizontal takeoff and landing flights within a wide speed range flight envelope, and it is a promising scheme with low cost and reusability for future supersonic/hypersonic aircraft [3]. Wherein the inlet system behaves as a crucial component and plays a vital role in the TBCC propulsion

[1] *School of Aerospace Engineering, Xiamen University, Xiamen, Fujian, 35020200156007@stu.xmu.edu.cn*
[2] *School of Aerospace Engineering, Xiamen University, Xiamen, Fujian, 35020230156550@stu.xmu.edu.cn*
[3] *AECC Sichuan Gas Turbine Establishment, Chengdu, Sichuan, 463224222@qq.com*
[4] *School of Aerospace Engineering, Xiamen University, Xiamen, Fujian, 35020220156443@stu.xmu.edu.cn*
[5] *School of Aerospace Engineering, Xiamen University, Xiamen, Fujian, 34520202200315@stu.xmu.edu.cn*
[6] *School of Aerospace Engineering, Xiamen University, Xiamen, Fujian, chengxiang.zhu@xmu.edu.cn*
[7] *School of Aerospace Engineering, Xiamen University, Xiamen, Fujian, yancheng.you@xmu.edu.cn*

system. Compared with traditional two-dimensional and axisymmetric TBCC inlets, the inward-turning TBCC inlet equips more advantages, such as small wetted area, strong compression efficiency, and high total pressure recovery [4-7], and has attracted much research attention [8-10].

Recently, researchers have conducted some studies on the different layouts of inward-turning TBCC inlets and revealed their aerodynamic performance. Zuo et al. [11] designed an over/under inward-turning TBCC inlet at $Ma_\infty=4$ and validated its fully captured capability of mass flow. They also simulated the mode transition process at $Ma_\infty=2.5$ by adjusting the movable compression surface, cowl, and splitter and pointed out that the inlet had an increasing total pressure recovery as the range of splitter angle decreased. Min et al. [12] studied the back pressure effect on the mass flow redistribution and distortion based on a three-channel inward-turning TBCC inlet, similar to the "Trijet" inlet [8]. Subsequently, Zhu et al. [13] provided an over/under tri-duct inward-turning inlet with a wide speed range from Mach 0 to 6, and a single rotational flap was set on the compression side to control the working modes transition. Their results indicated that the inlet worked properly at low flight speeds and overcame the starting problem. Zhu et al. [14] and He et al. [15] both designed the adjustable over/under inward-turning TBCC inlets and discussed the inlets' starting problem at low speed, and He [15] further investigated the influence on the outlet performance and outlet distortion caused by the change rule of the centerline. Zhu et al. [16], Kong [17], and Cai et al. [18] designed and studied the tetra-duct inward-turning inlets, and they pointed out their inlets' low-speed experimental performance, aerodynamic performance within the full speed range, and mass flow characteristics, respectively. Moreover, Huang [19] and Hu et al. [20] explored the mode transition process of the inward-turning TBCC inlet, demonstrating the effects of geometric structure, Mach number, respectively.

These previous inward-turning TBCC inlet schemes have deepened our understanding of the inward-turning TBCC inlet and proved that the inward-turning TBCC inlet exhibited noteworthy advantages that merit thorough investigation [21]. However, most of the research work is still in the stage of numerical simulation to date, and few studies have installed the inward-turning TBCC inlet in the wind tunnel for experimental research. Although Zhang [22] and Zhu [16] both conducted the wind tunnel tests on the inward-turning inlet, the performance at the design point under the test conditions has never been introduced in their work. Therefore, the current research necessitates broadening the design concept for the inward-turning TBCC inlet and conducting relevant experimental validations to address the deficiencies in this area of study, thereby deepening and strengthening our understanding on that.

In this study, we focus on the wind tunnel test on an inward-turning TBCC inlet, which was designed based on the two-stage compression basic flow field, aiming to validate the design concept and obtain the aerodynamic performance of the TBCC inlet under different working modes. The paper is organized as follows: Section 2 briefly introduces the design concept and inlet model of the inward-turning TBCC inlet. The description of the wind tunnel and test data acquisition system are subsequently described in Section 3. Section 4 shows the experimental results and comparison with the numerical results. Conclusions and future research directions are outlined in Section 5.

2. Model design and method description

2.1. Design concept of inward-turning TBCC inlet

First, the design concept of the inlet is briefly introduced. In this work, we tried a novel design concept to design the inward-turning TBCC inlet by utilizing the two-stage compression basic flow field, as illustrated in Fig. 1. The configuration of the basic flow field is shown in Fig. 1 (a), two incident shock waves and a reflected shock wave decelerate and pressurize the freestream. Fig. 1 (b) and (c) display the design steps of the inward-turning TBCC inlet:

Step 1: Generate the inlet aerodynamic profiles. As shown in Fig. 1 (b), the profile of the inward-turning inlet at the design point is generated by streamline tracing technology. At the design point, the mass flow can be fully captured owing to the incident shock that can accurately hit the cowl point. The two incident shock waves compress and pressurizes the airflow for the inward-turning inlet, trending to shorten the compression length and improve the compression capacity, and that has been verified by Li [23].

Step 2: Design the variable geometry structure. The low-speed turbine duct needs to be designed on the basis of the obtained inward-turning inlet profile, where the schematic diagrams are presented in Fig. 1 (c). In the present design concept, we define the second-stage compression surface and second-

stage compression angle as adjustable splitter and rotation angle, respectively. Rotating the second-stage compression surface to parallel to the first-stage compression surface to generate the entrance of the turbine duct. It provides an efficient method in designing the hinge location and rotation angle of the splitter. Furthermore, when the splitter is rotated parallel to the first-stage compression surface under turbine mode, there is only a single incident shock wave and reflected shock wave in the compression segment. The expansion phenomenon, which will inevitably occur at the hinge in the traditional design concept, also can be weakened or even avoided in the present design concept. In this model, this adjustable feature of the second-stage compression wall not only governs the opening and closing of the turbine duct but also plays a pivotal role in regulating the inlet's contraction ratio. This dual functionality ensures the inlet's smooth and efficient operation across different conditions.
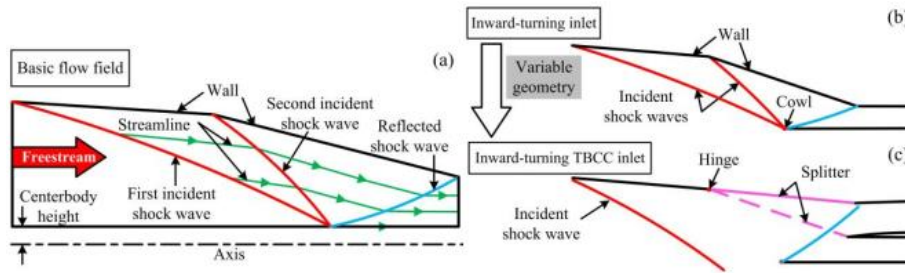
Fig 1. Schematic diagram of inward-turning TBCC inlet with double incident shock wave.

2.2. Solution method of the basic flow field

As shown in Fig. 2, the basic flow field with double incident shock waves is divided into six separate domains for the solution according to its shock wave structure, including shock-dependent domains (①, ③, ⑤) and isentropic compression domains (②, ④, ⑥). The shock wave AO and shock-dependent domain ① (AOB) can be solved when the free stream parameters, center body height, and the first-stage compression angle δ_1 are known. Extend point B to point B', and solve the domain BOB' according to the isentropic conditions. Subsequently, according to the second-stage compression angle δ_2, iterate the starting point C of the second-stage compression wall on the wall BB' until the shock wave CO intersects with shock wave AO at point O. When point C is determined, the isentropic compression domain ② (BOC) and shock-dependent domain ③ (COD) can be obtained. Similarly, extend point D to point D' and solve the isentropic compression domain DOD'. Then, the reflected shock wave EO, isentropic compression domain ④ (DOE), and shock-dependent domain ⑤ (EOF) can be solved by giving the horizontal center body OF. Finally, the domain ⑥ (EFG) also can be obtained by extending point F to point G. Here, the black dashed lines BO, B'O, and DO are right-running characteristic lines C_-, and the green dashed lines D'O and EF are the left-running characteristic lines C_+.
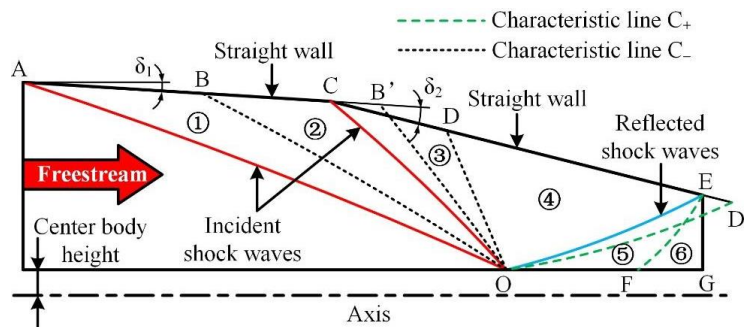
Fig 2. Solution method of the basic flow field with two incident shock waves.

In this process, the Method of Curved-shock Characteristics (MOCC) [24-25] is employed to solve the inviscid basic flow field. It only requires one streamline and one characteristic line to solve the basic flow field, owing to more aerodynamic parameters that can be obtained according to the curved shock theory. Fig. 3 (a) shows the step process of MOCC for the shock-dependent domain ① when the free stream parameters and compression wall are given, where $A_1, A_2...A_n$ are discrete points on the given wall and $B_1, B_2...B_n$ are discrete points of the shock wave solved, respectively. The isentropic compression domain BOB' subsequently is solved combined with the isentropic condition and MOCC by giving the wall BB'. While the shock-dependent domain ③ needs to be solved iteratively, as stated

above, due to the starting point C of the second-stage compression wall that needs to be determined to control that the second incident shock wave also converges at point O. Different from the domain ①, the airflow parameters before the second incident shock wave are obtained by interpolating in domain BOB', but the step process for solving the basic flow field parameters keeps consistent, as illustrated in Fig. 3 (a). Once the domain ③ is determined, the isentropic compression domain DOD' also can be solved by giving the wall DD' refer to the solution method in domain BOB'.
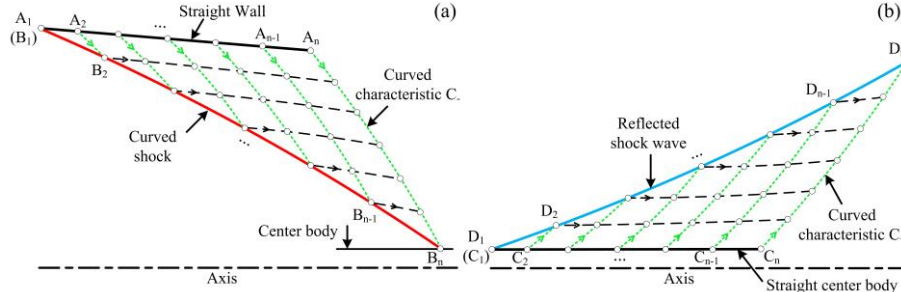
Fig 3. Step process of MOCC under the condition of the given wall. (a) incident shock-dependent domain. (b) reflected shock-dependent domain.

Similarly, the reflected shock-dependent domain ⑤ is solved according to the straight center body wall, here the airflow parameters before the reflected shock wave are obtained by interpolating in domain DOD', and the step process is shown in Fig. 3 (b). In this domain, the streamline and characteristic line C_+ are employed to solve the basic flow field parameters, where $C_1, C_2...C_n$ are discrete points on the center body wall and $D_1, D_2...D_n$ are discrete points of the reflected shock wave solved. Finally, the whole basic flow field can be obtained by solving the domain ⑥ according to the wall FG, the parameters along the EF, and the isentropic condition.

2.3. Aerodynamic model design

According to the above design concept, an inward-turning TBCC inlet was designed at design point $Ma_\infty=4$, which operated within the Mach numbers ranging from 0 to 4. Wherein the turbine mode ranges from Mach number 0 to 3 and the ramjet mode ranges from 3 to 4, featuring a mode transition Mach number of 3. Furthermore, according to the engines' requirements, the ramjet duct is required to commence operation at Mach number 2. It indicates that the turbine and ramjet ducts operate together at the speed range $Ma_\infty=2\sim3$.

The two-stage compression basic flow field was designed at design point $Ma_\infty=4$, and Table 1 provides the relevant design parameters. Here, the compression walls of the basic flow field are configured as straight walls, where δ_1 and δ_2 denote the compression angles. Additionally, H_C represents the height of the center body, and the parameters Ma_∞, p_∞ and ρ_∞ specify the freestream Mach number, static pressure, and density, respectively.

**Table 1.** Design parameters of the basic flow field

Ma_∞	p_∞ (kPa)	ρ_∞ (kg/m³)	δ_1	δ_2	H_C
4.0	4.51	0.072	5	11	0.16

Fig. 4 compares the pressure distribution of the inviscid basic flow field between the MOCC results and Computational Fluid Dynamics (CFD) results, represented by the red dashed line and black solid line, respectively. Clearly, the shock waves and pressure distribution calculated by the MOCC exhibit negligible errors in comparison to the CFD results. The high accuracy demonstrated by MOCC renders the solved basic flow field suitable and reliable for the design of the inward-turning inlet.

Subsequently, an approximate rectangular entrance shape was selected to trace the compression segment in consideration of an easier implementation of the adjustable second-stage compression wall on the compression segment, as displayed in Fig. 5 (a). As the design concept described above, the adjustable second-stage compression wall, namely the splitter I, was designed on the compression segment. Rotating the splitter I around the hinge T_1 to parallel to the first-stage compression surface, the rectangular entrance of the turbine duct will be conveniently obtained. The coefficients of the

centerline equation and the cross-section area equation are selected ϕ_2 and ϕ_3 [26] respectively to design the expansion ducts. In addition, an adjustable splitter II was set on the turbine duct to control the opening and closing of the turbine duct.
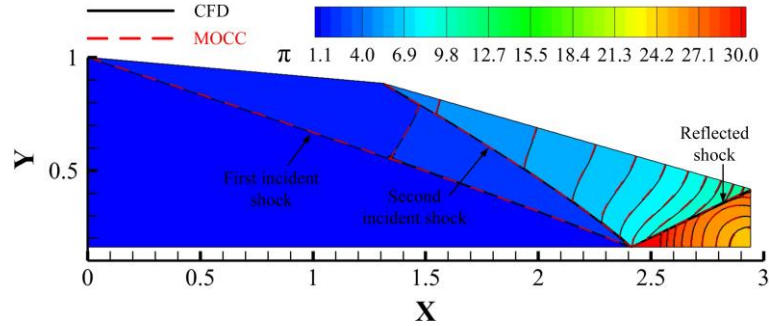
Fig 4. Pressure distribution of the basic flow field with double incident shock waves.
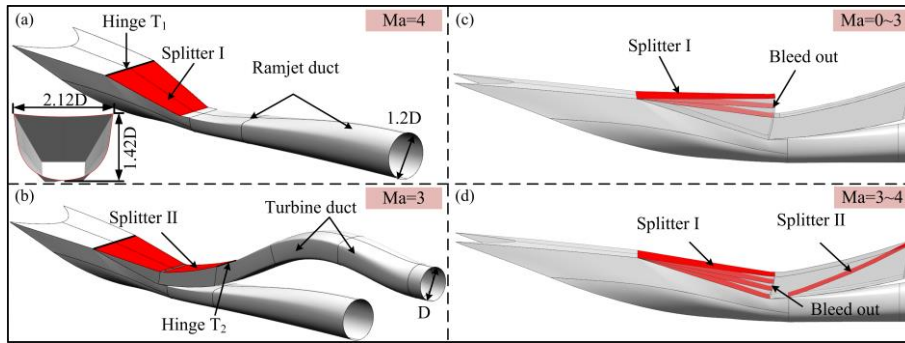
Fig 5. Aerodynamic model of the inward-turning TBCC inlet.

Fig. 5 (c) and (d) present the regulation of the variable geometry structures under different working conditions. At the turbine mode $Ma_\infty=0\sim3$, the splitter I rotates upward to weaken the compression and ensure the starting of the inlet, and the splitter I is parallel to the first-stage compression surface at $Ma_\infty=3$. When the inlet transitions to ramjet mode $Ma_\infty=3\sim4$, the turbine duct is fully closed by the splitter II, and the splitter I is gradually closed from Mach number 3 to 4.

2.4. Numerical method

Before conducting the wind tunnel test, steady numerical simulations were carried out to investigate the inlet's aerodynamic performance by utilizing the commercial software ANSYS FLUENT. In this work, the computational domain grids under different working conditions were generated by the software ANSYS ICEM. The refined near-wall grid ensured the precision of solutions within the near-wall boundary layer, where the dimensionless wall distance y^+ of the first grid was maintained below 1.0. In simulations, the density-based three-dimensional Reynolds-average Navier-Stokes (RANS) equations solver was adopted. The airflow was treated as the ideal gas, the piecewise polynomial method was chosen to compute specific heat, and the viscosity was calculated by Sutherland's law [28]. In addition, the two-equation k-ω shear stress transport (SST) [27] was employed to simulate the turbulence flow. The 2nd-order upwind Roe-flux-difference split-ting (Roe-FDS) scheme was applied for the flux term, and the least squares cell-based method was employed to evaluate the gradient of flow parameters.

3. Experimental setup

3.1. Wind tunnel and test model

In this work, the wind tunnel tests were conducted at a 1.2m × 1.2m (width × height) supersonic wind tunnel. It can provide the stable subsonic or supersonic freestream more than 20s within the speed range of Mach 0.3 to 4.2, and its lengths of the transonic and supersonic test sections are 3.8m and 2.2m, respectively.

Building upon the aerodynamic model of the inward-turning TBCC inlet shown in Fig. 5, we manufactured a scaled inward-turning TBCC inlet model for the wind tunnel test, where the total length of the inlet was 1028mm, and the outlet diameters of the turbine and ramjet ducts are 62.5mm and

75mm, respectively. Fig. 6 illustrates the inverted installation of the inlet test model within the test section of the wind tunnel. The cowl side was oriented upward, and the connection be-tween this side and the wind tunnel was established using a right-deflected β board. In addition, to obtain the wall static pressure, there were two sets of pressure measurement points positioned along the inlet test model: one set on the upper side of the turbine duct and another on the lower side of the ramjet duct.


Fig 6. Test model of the inward-turning TBCC inlet in the wind tunnel.

3.2. Data acquisition and processing

During the tests, the high-speed schlieren system was employed to capture the flow structure at the inlet's entrance, which played a crucial role in offering a visual assessment of the inlet's starting status. In addition, the PSI8400 series pressure scanner system was employed to record wall static pressure and outlet total pressure, and its range and measurement accuracy were 0~30 PSI and ±0.05% FS (full scale), respectively.

To obtain the outlet's aerodynamic performance, the constant area measurement sections were connected downstream of the turbine/ramjet duct outlet, respectively. In each measurement section, the measurement points were organized into eight rakes with an equal-area distribution, and the layout of the rake array is illustrated in Fig. 7. Each rake is furnished with five steady-state total pressure measurement points. At the radius of 90%, we set four Kulite sensors with a sampling frequency of 20kHz, represented by uppercase letters A, B, C, and D, to record the dynamic total pressure. Along the circumferential wall, four static pressure measurement points, represented by numbers 1, 2, 3, and 4 in the figure, are placed.
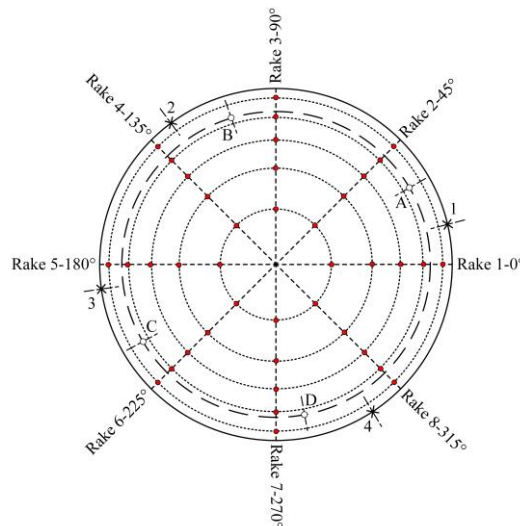
Fig 7. Rake array inside the measurement section.

To investigate the inlet performance under different back pressure and the critical state, the mass-flow throttle plug was set behind the measurement section of the turbine/ramjet duct to simulate the back pressure caused by combustion, and it was driven by a stepper motor. The throttling ratio (TR) is defined to represent the axial position of the plug [29]:

$$TR = (1 - A_{th,plug}/A_{exit}) \times 100\% \qquad (3)$$

where $A_{th,plug}$ and A_{exit} represent the plug throat area and duct outlet area, respectively. During the tests, varying back pressure can be achieved by adjusting the value of TR.

In processing the experimental data, we defined several parameters to represent the inlet's aerodynamic performance, mainly including outlet pressure ratio π_k, total pressure recovery coefficient σ_{exit}, and outlet Mach number Ma_{exit}. As follows, the parameters π_k, σ_{exit}, and Ma_{exit} were defined as:

$$\pi_k = \frac{P_{exit,ave}}{P_\infty}, \ P_{exit,ave} = \frac{1}{n}\sum_{j=1}^{n} P_{exit,j} \qquad (4)$$

$$\sigma_{exit} = \frac{P_{t,ave}}{P_{t,\infty}}, \ P_{t,ave} = \frac{\sum_{i=1}^{m} P_{t,i}\ \Delta A_i}{A} = \frac{1}{m}\sum_{i=1}^{m} P_{t,i} \qquad (5)$$

$$Ma_{exit} = \sqrt{5\left(\pi_s^{-\frac{2}{7}} - 1\right)}, \ \pi_s = \frac{P_{exit,ave}}{P_{t,\infty}} \qquad (6)$$

where "n" was the number of static pressure measurement points, and $P_{exit,j}$ and P_∞ represent the outlet static pressure at the measurement point and freestream static pressure, respectively. "m" was the number of total pressure measurement points at outlet, and $P_{t,i}$ and $P_{t,\infty}$ denote the total pressure captured by the measurement point and freestream total pressure.

4. Results and discussion

This section mainly presents the wind tunnel test results of the inward-turning TBCC inlet. First, the experimental results at design point $Ma_\infty=4$ are discussed and compared with simulation results. Subsequently, we present some experimental results under off-design points to assess the aerodynamic performance of the inlet under different working modes.

4.1. Test results at design point $Ma_\infty=4$

As illustrated in Fig. 8, the schlieren system captured the flow structure at the inlet's entrance under design point $Ma_\infty=4$. During the test, with the value of TR gradually increasing to 70%, the shock structure observed remained stable, and no other shock waves appeared, which indicated the inlet kept starting and normally operating. However, the stable shock structure was quickly destroyed when the value of TR continued to increase, as displayed in Fig. 8 (b). By referring to the schlieren images, we successfully observed the entire process of the inward-turning TBCC inlet from starting to unstart and obtained the critical working condition of the inlet under the design point.
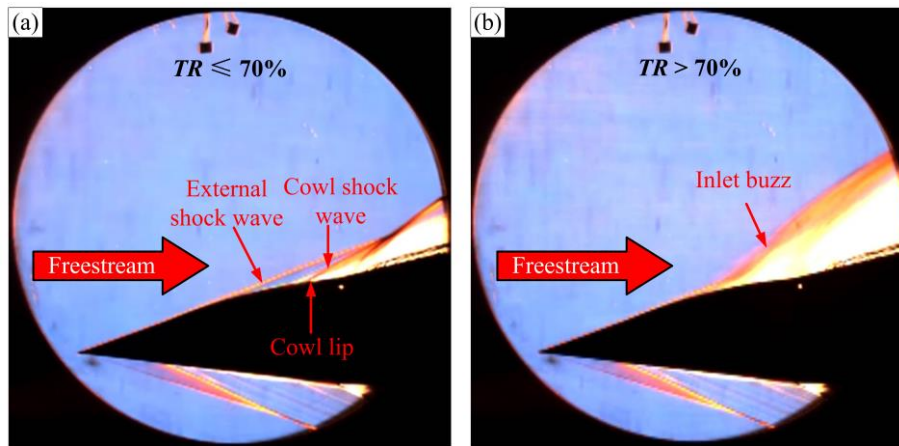
Fig 8. Schlieren images of the inlet at design point $Ma_\infty=4$

The static pressure ratio distributions along the inlet wall under different TR values are given in Fig. 9, where P/P_∞ and X/L represent the dimensionless pressure ratio and relative position, respectively. Fig.

9 (a) describes the static pressure ratio on the lower wall of the ramjet duct side, while Fig. 9(b) only displays the static pressure ratio measured on the compression wall of the inlet.
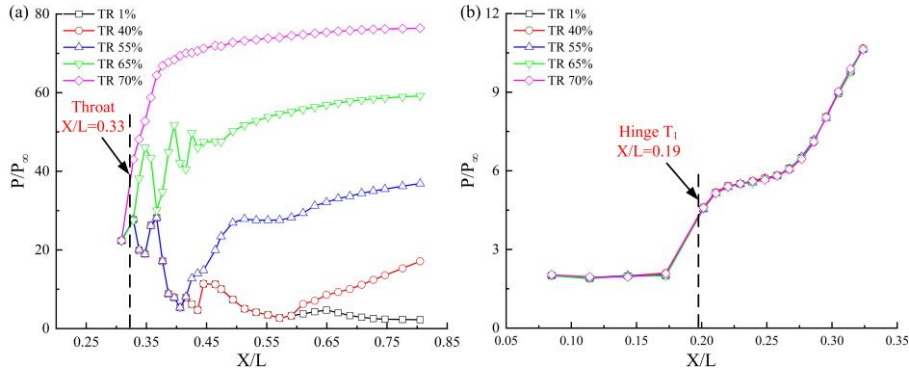
Fig 9. Static pressure distribution along the wall at Ma$_\infty$=4. (a) lower wall. (b) upper wall.

As the TR value gradually increased to 40%, the terminal shock wave formed and gradually moved forward within the ramjet duct in this process, noticeable through the sudden rise in static pressure ratio in Fig. 9(a). Subsequently, with the TR value increased from 40% to 70%, the position of the terminal shock kept moving forward. Notably, at the TR value of 70%, the terminal shock was positioned remarkably close to X/L=0.33, almost at the inlet throat. This particular condition put the inlet in a critical state, making it prone to unstart if the terminal shock wave crossed the throat due to back pressure. However, the measured static pressure ratio on the upper wall remained almost constant, as displayed in Fig. 9(b), owing to the terminal shock wave not affecting the flow field front of the throat when the TR value was less than 70%. At about X/L=0.19 along the upper wall, the measured static pressure abrupt rise reflected the second incident shock wave in the compression segment, which reveals the two-stage compression characteristic of the inlet. Test results indicate that, as the TR value increased, the back pressure ratio at the outlet exhibited a gradual rise from 7.76 to 76.56, accompanied by a decrease in the outlet Mach number from 2.28 to 0.161. However, the total pressure recovery coefficient first decreased from 0.611 to 0.229 as the TR value increased from 1% to 40%, subsequently showing a gradual increase to the critical value of 0.506 when the TR value increased from 40% to 70%.

## 4.2. Comparison with simulation results

First, the wall static pressure ratios between the experimental and numerical results are compared to validate the numerical method and results, as shown in Fig 10. Here, the experimental results of the lower wall static pressure ratio at TR=55%, 65%, and 70% are selected to compare with the numerical back pressure ratios π_k=39.83, 60.08, and 76.03, respectively, where the Y-axis P/P$_\infty$ only represents the dimensionless value of the pressure ratio. As depicted in the figures, the experimental pressure ratios agree well with numerical results, exhibiting agreement on the terminal shock position and overall trend. The pressure ratio comparison on the upper wall between TR=55% and π_k=39.83 is shown in Fig. 10(b), where the numerical pressure ratios closely align with the experimental results, fully proving the reliability of the numerical results shown in Fig. 10 (c)~(e).

Furthermore, the quantitative comparison of the outlet performance parameters under different back pressure ratios is displayed in Fig. 11. In the figure, the X-axis represents the dimensionless outlet pressure ratio in test (Exp-π_k) or simulation (Num-π_b), and the Y-axis σ_{exit} and $M_{a\,exit}$ represents the total pressure recovery coefficient and outlet Mach number, respectively. Overall, the numerical results demonstrate a high degree of consistency with the experimental results regarding the total pressure recovery coefficient and outlet Mach number, both in terms of trend and values. For an instance, π_k =38.99, $\sigma_{exit,exp}$ =0.281, and $Ma_{exit,exp}$ =0.386 at TR=55%, while $\sigma_{exit,num}$ =0.292 and $Ma_{exit,num}$=0.32 at π_b=39.83 in simulation. In addition, the performance difference under the critical state is quite small in this inlet, where π_k=76.56, $\sigma_{exit,exp}$=0.506, and $Ma_{exit,exp}$=0.16 at TR=70% in the test, and $\sigma_{exit,num}$=0.505 and $Ma_{exit,num}$=0.20 at π_b=76.03 in simulation. The wind tunnel test under the design point Ma$_\infty$=4 illuminated the aerodynamic performance and critical state of the inlet, validating the design concept of the two-stage compression inward-turning inlet.
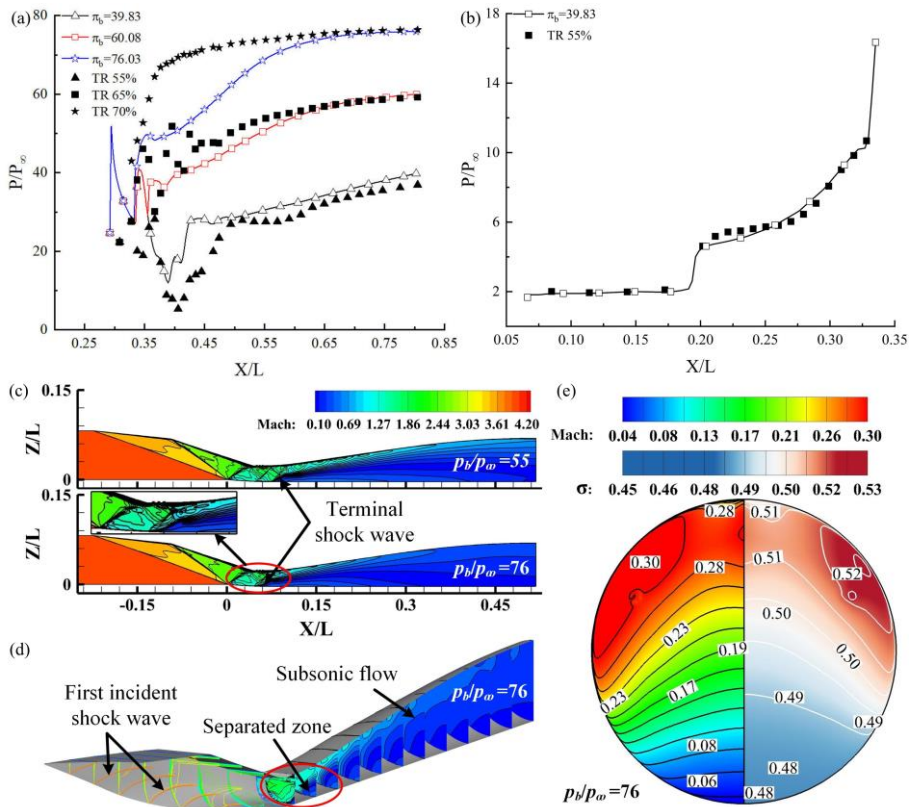
Fig 10. Static pressure comparison between the experimental and numerical results at Ma$_\infty$=4. (a) lower wall. (b) upper wall. (c)~(e) simulation results
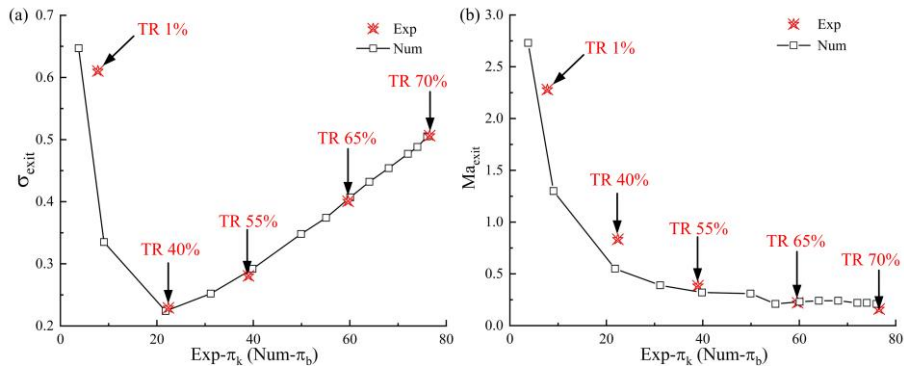

Fig 11. Performance parameters comparison between the experimental and numerical results at Ma$_\infty$=4. (a) total pressure recovery coefficient. (b) Mach number at outlet.

4.3. Aerodynamic performance under off-design points

In assessing the inward-turning TBCC inlet, beyond confirming its performance under the design point, it's equally essential to ensure its working performance across off-design points throughout the speed range. This comprehensive evaluation is critical for gauging the aerodynamic design of the inward-turning TBCC inlet. Therefore, wind tunnel tests were conducted on this model under different off-design points, including subsonic Ma$_\infty$=0.8, supersonic Ma$_\infty$=2, 3.

The static pressure ratio distributions along the inlet wall at Ma$_\infty$=0.8 are shown in Fig. 12, where figures (a) and (b) represent the turbine and ramjet sides, respectively. Additionally, numerical static pressure ratio distributions under different π_b values are also displayed in the figures to compare with the experimental results. Fig. 12(a) reflects the position of the terminal shock wave under the different TR values, reaching the throat at TR=65%, at which time the inlet worked in a critical state. At the lower side wall of the ramjet duct, the pressure ratio variation trend indicated that when TR=1%, a

shock wave was present in the duct, while it won't affect the turbine duct at this constant TR value. Under this condition, the maximum back pressure ratio of the experimental results is 1.386, which is slightly higher than the 1.35 of simulation results. The corresponding critical total pressure recovery coefficients are 0.952 and 0.975, respectively.
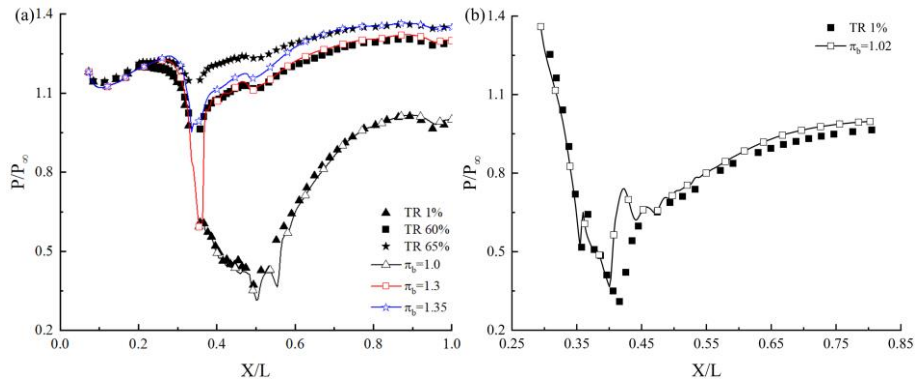

Fig 12. Static pressure distribution along the wall of the inlet at subsonic condition at Ma_∞=0.8. (a) upper wall. (b) lower wall.

Fig. 13 displays the flow structure at the inlet's entrance captured by the schlieren system at turbine mode Ma_∞=2, and the flow structure remained unchanged when the inlet normally worked. Under this working condition, both the turbine and ramjet ducts were operating, and the TR values on the two ducts were both changed during the test, aiming to obtain the critical state of each duct. Results indicated that the maximum TR values of the turbine and ramjet ducts were 67% and 71%, and the corresponding maximum back pressure ratios were $\pi_{k,\ T}$=6.84 and $\pi_{k,\ R}$=6.27, where the subscripts "T" and "R" represent the turbine and ramjet ducts, respectively.
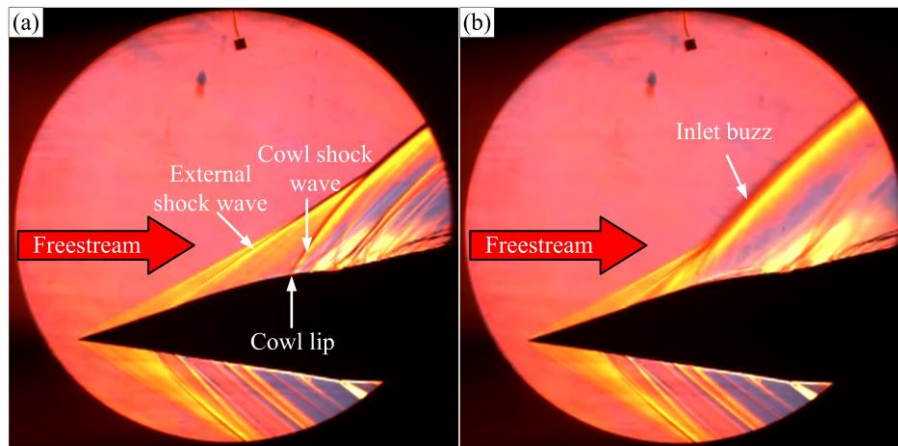

Fig 13. Schlieren images of the inlet at off-design point Ma_∞=0.8.

In this test, the back pressure characteristics of the inward-turning TBCC inlet under turbine mode Ma_∞=2 were clarified by varying the TR value. As the back pressure ratio increased, the total pressure recovery of both ducts initially decreased before increasing, while the outlet Mach number gradually declined. These trends are consistent with the simulation results, as depicted in Fig. 14. Among the test results, the critical total pressure coefficient and outlet Mach number of the turbine duct were 0.903 and 0.34 at $\pi_{k,\ T}$=6.84, and those were 0.795 and 0.235 of the ramjet duct at $\pi_{k,\ R}$=6.27, respectively. The obtained experimental characteristics and performance under the condition of both ducts working at the same time will help deepen the cognition of inward-turning TBCC inlets, and this research work has important guiding significance for inlet optimization design and engineering application.
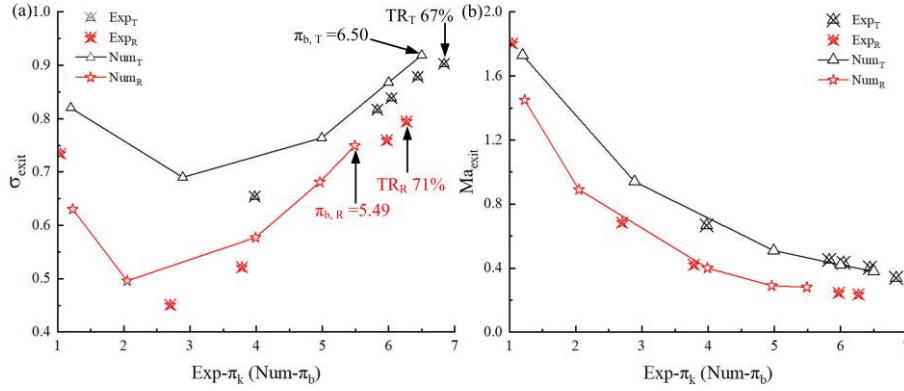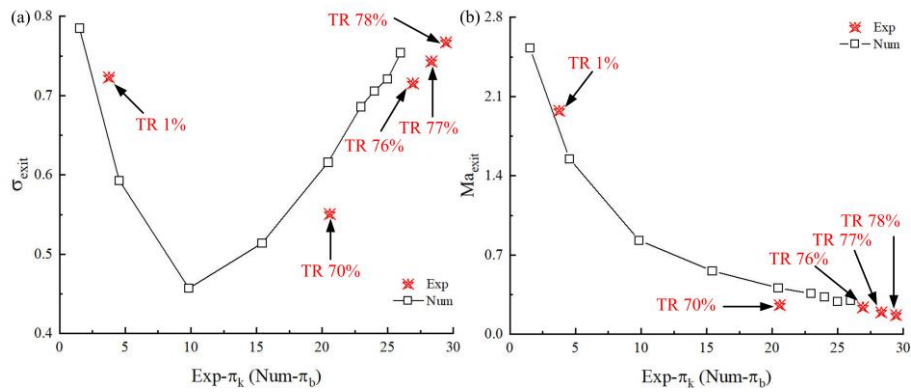
Fig 14. Performance parameters comparison between the experimental and numerical results at turbine mode $Ma_\infty=2$. (a) total pressure recovery coefficient. (b) Mach number at outlet.

During the test conducted at ramjet mode $Ma_\infty=3$, the splitter II on the turbine duct was fully closed, while the splitter I was not completely closed, as shown in Fig. 5(d). Fig. 15(a) displays the flow structure at the entrance under the starting state of the inlet, and this stable flow structure was disrupted when the TR value exceeded 78% during the test. In addition, the wall static pressure ratios between experimental and numerical results agree well on the upper and lower wall under a similar back pressure ratio, as illustrated in Fig. 15(b), where π_k and π_b are 26.91 and 25.98, respectively. On the upper wall, the sudden increase in pressure ratio at about X/L=0.19 reflected the second incident shock wave formed by the splitter I, which was similar to that at $Ma_\infty=4$ in Fig. 9(b), highlighting the two-stage compression characteristic of the inlet. The static pressure ratio distribution on the lower wall pointed out the position of the terminal shock wave near the throat, showing a close agreement with the simulation results.
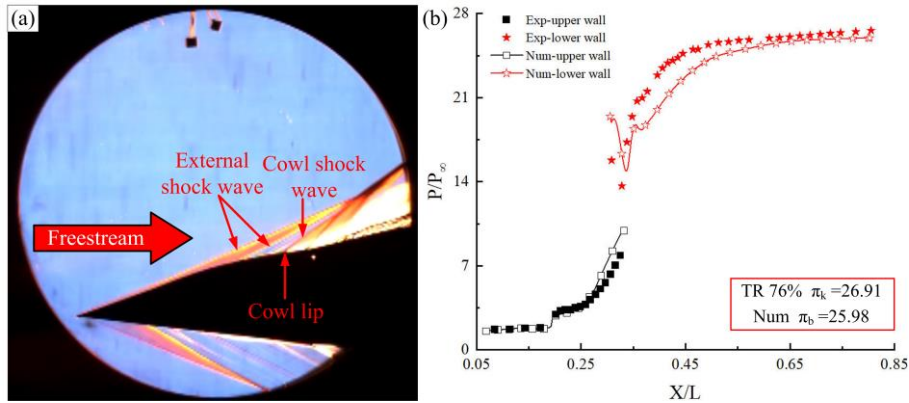
Fig 15. Experimental results of the inlet at ramjet mode $Ma_\infty=2$. (a) schlieren image at the entrance. (b) wall static pressure ratio distribution.

Fig. 16 presents the back pressure characteristic of the ramjet duct at $Ma_\infty=3$. As the back pressure ratio increased to maximum back pressure ratio $\pi_k=29.44$, the experimental total pressure recovery coefficient of the ramjet duct dropped from 0.723 to 0.551 and finally increased to 0.762, while the outlet Mach number continuously declined from 1.87 to 0.17, which shows a consistent trend to that described on the ramjet duct under the condition $Ma_\infty=2$. In simulation results, the total pressure recovery coefficient and outlet Mach number are 0.754 and 0.3 under the maximum back pressure $\pi_b=25.98$. The maximum back pressure ratio in this condition also behaved a little higher than that in simulation, and the reason is explained above and not repeated here.

Fig 16. Performance parameters comparison between the experimental and numerical results at ramjet mode Ma$_\infty$=3. (a) total pressure recovery coefficient. (b) Mach number at outlet.

In general, we present the experimental performance and back pressure characteristics of the inward-turning TBCC inlet under the design point and some off-design points. Moreover, the experimental results are compared with the numerical results at each test condition, encompassing the wall pressure ratio distribution and outlet parameters, all of which exhibit commendable consistency. These detailed comparisons greatly enhance the accuracy and reliability of the wind tunnel test results. Simultaneously, the design method of the inward-turning TBCC inlet based on the two-stage compression basic flow field has been validated through the wind tunnel tests and the experimental results.

5. Conclusions

In this study, an inward-turning TBCC inlet was designed based on the two-stage compression basic flow field and tested on the wind tunnel under design and off-design points. The observed flow structure and measured pressure date reveal its working features and back pressure characteristics within the designed speed range. Some main conclusions established under experimental results are drawn as follows:

(1) At the design point Ma$_\infty$=4, the inlet can self-start and work stably. The experimental pressure ratio distributions along the upper wall agree well with the numerical results, demonstrating the same shock wave structure in the symmetry plane. Results prove the inlet's two-stage compression characteristic and validate the design concept.

(2) The inlet has good aerodynamic performance across the wide speed range. At subsonic Ma$_\infty$=0.8, the turbine duct's maximum total pressure recovery coefficient can reach 0.959. When the Mach number increased to Ma$_\infty$=2, the turbine duct's maximum total pressure recovery coefficient dropped to 0.903, while that of the ramjet duct was 0.795. Under the ramjet mode, the maximum total pressure recovery coefficient decreased from 0.754 to 0.506 as the Mach number increased from 3 to 4, and the ramjet duct's maximum back pressure ratio was 76.56 under the design point.

(3) The remarkable consistency between the experimental and numerical results, particularly in terms of the distribution of wall pressure ratios and outlet performance, serves as a robust validation of the study methodology. That significantly enhances the credibility of the aerodynamic performance of the inlet across a wide speed range. Crucially, the efficacy of the inlet's design concept, as presented in this paper, is duly affirmed by combining the experimental and simulation results.

The current study investigated the inlet's aerodynamic performance under different conditions through the wind tunnel test, which can widen the design idea of the TBCC inlet and promote its engineering application. In the future, further research on the design method and flow mechanism will be carried out to deepen the understanding of the inward-turning TBCC inlet.

References

1. Snyder L, Escher D, Defrancesco R, Gutierrez J, Buckwalter D.: Turbine based combination cycle (TBCC) propulsion subsystem integration. Report No.: AIAA -2004-3649 (2004)

2. Chen M, Tang HL, Zhu ZL.: Goal programming for stable mode transition in tandem turbo-ramjet engines. Chin J Aeronaut. 22(5): 486–92 (2009)

3. James McDaniel, Chris Goyne, Jack Edwards, Harsha Chelliah, Andrew Cutler, Peyman Givi.: US national Center for hypersonic combined cycle propulsion: An overview. Report No.: AIAA-2009-7280 (2009)

4. You YC.: An overview of the advantages and concerns of hypersonic inward turning inlets. Report No.: AIAA-2011-2269 (2011)

5. Qiao WY, Yu AY, Gao W, et al.: Design method with controllable velocity direction at throat for inward-turning inlets. Chin J Aeronaut. 32(6): 1403-1415 (2019)

6. Li YM, Li ZF, Yang JM.: Tomography-like flow visualization of a hypersonic inward-turning inlet. Chin J Aeronaut. 34(1): 44-49 (2021)

7. Yin ZY, You YC, Zhu cx, et al.: Multi-ducted twin-turbines ejector-ramjet/scramjet combined cycle engine for hypersonic civil vehicles. Acta Aeronautica et Astronautica Sinica. 44(02):7-19 (2023)

8. Siebenhaar A, Bogar T.: Integration and vehicle performance assessment of the Aerojet "TriJet" combined-cycle engine. Report No.: AIAA-2009-7420 (2009)

9. He XZ, Zhou Z, Qin S, et al.: Design and experimental study of a practical osculating inward cone waverider inlet. Chin J Aeronaut. 29(6): 1582-1590 (2016)

10. Zuo FY, Mölder S.: Hypersonic wavecatcher intakes and variable-geometry turbine based combined cycle engines. Progress in Aerospace Sciences. 106: 108-144 (2019)

11. Zuo FY, Huang GP, Chen J, Tang WY.: Based on the concept of waverider TBCC inlet mode transition study. J Eng Thermophysics. 36(02):274-278 (2015)

12. Min H, Sun B, Li JX, Wu FL, Zhang KY.: Investigation on interference characteristics among channels of a over-under inward turning inlet. J Propulsion Technology. 39(12): 2695-2702 (2018)

13. Zhu CX, Zhang X, Kong F, You YC.: Design of a three-dimensional hypersonic inward-turning inlet with tri-ducts for combined cycle engines. Int J Aerospace Eng (2018). https://doi.org/10.1155/2018/7459141

14. Zhu W, Wang X, Hua ZX, et al.: The design and analysis of wide speed range turbine based combine cycle three-dimensional inward turning inlet. Aircraft Design. 39(03):13-17+38 (2019)

15. He MF, Li XK, Yin C, et al.: Aerodynamic design and analysis of a TBCC inlet based on inward-turning inlet. Aircraft Design. 41(04):56-64+73 (2021)

16. Zhu CX, Zhang HF, Hu ZC, You YC. Analysis on the low speed performance of an inward-turning multiduct inlet for turbine-based combined cycle engines. Int J Aerospace Eng (2019). https://doi.org/10.1155/2019/6728387

17. Kong F.: Mass flow distribution design and performance analysis of multi-duct combine cycle inlet [dissertation]. Xiamen: Xiamen University (2019)

18. Cai ZJ, Hu ZC, Yu LC, Hong TB, Zhu CX, You YC.: Design concept and aerodynamic characteristics of XTER TBCC inlet. Acta Aerodynamic Sinica. 40(1): 218-231 (2022)

19. Huang XF.: Study on flow characteristics of mode transition of the over-under adjustable TBCC inward-turning inlet [dissertation]. Nanjing: Nanjing University of Science and Technology (2018)

20. Hu ZC, Cai ZJ, Wang TY, Zhu CX, Wu LN, You YC.: Analysis of effects of mode transition type on performance of mode transition for 3D inward-turning combined inlet. J Propulsion Technology. 41(12): 2670-2680 (2020)

21. Hou X.: Research Progress in combined cycle engines. Acta Aeronautica et Astronautica Sinica. 44(21):35-47 (2023)

22. Zhang X.: Research on design technology of three-dimensional inward turning TBCC inlet [dissertation]. Xiamen: Xiamen University (2019)

23. Li YZ, Zhang KY, Zhu W, Yang SK.: Design for inward turning basic flowfield with controlled center body and two incident curved shock waves. J Aerospace Power. 30 (3):563-570 (2015)

24. Shi CG, Zhu CX, You YC, Zhu GS.: Method of curved-shock characteristics with application to inverse design of supersonic flowfields. J Fluid Mechanics. 920: A36 (2021)

25. Tang YQ, Shi CG, Zheng XG, Zhu CX, You YC.: Design and analysis of two-stage compression internal flowfield based on Method of Curved-Shock Characteristics. Physics of Gases. 7 (6): 42-54 (2022)

26. Lee C, Boedicker C.: Subsonic diffuser design and performance for advanced fighter aircraft. Aircraft Design Systems and Operations Meeting (1985)

27. Menter FR.: Two-equation eddy-viscosity turbulence models for engineering applications. AIAA J. 32(08): 1598–1605 (1994)

28. White FM.: Viscous fluid flow. New York: McGraw-Hill; 1974.p. 28–32.

29. Yuan HC, Li Z, Zhang JS.: Experimental and numerical research on a three-dimensional inward-turning inlet. J Aerospace Engineering. 36(3): 04023008 (2023)